RSC Advances

PAPER

View Article Online
View Journal | View Issue

Cite this: *RSC Adv.*, 2025, **15**, 38836

Structural, optical, vibrational, and dielectric properties of an Ni^{2+}-doped Sr_2MnWO_6 double perovskite for wireless applications

Jamal Shah,[a] Asad Ali, *[b] Tanveer Ahmad,[a] Alamgir Khan,[a] Salah Knani,[c] Vineet Tirth, [de] Ali Algahtani[df] and Abid Zaman *[g]

This study examined the effects of Ni^{2+} substitution on the structural, microstructural, optical, and dielectric properties of $Sr_2(Mn_{1-x}Ni_x)WO_6$ ($0.00 \leq x \leq 0.40$) double perovskites using a normal processing approach. Each sample's monoclinic structure and space group ($P21/n$) were verified using the X-ray diffractometry (XRD) technique. Successful ionic substitution was indicated by the XRD results, which showed a systematic drop in lattice parameters and unit cell volume with increasing Ni^{2+} content. Along with a rise in the lattice strain and dislocation density, the average crystallite size shrank from 58 nm (x = 0.00) to 47 nm (x = 0.40), indicating increased structural deformation. Images from scanning electron microscopy (SEM) revealed dense, crystalline microstructures with average grain sizes that gradually decreased as the Ni^{2+} content increased. This might be explained by the difference in the ionic radii between the host and substitution elements. With Ni^{2+} concentrations, the band gap energy increased from 3.10 eV to 3.51 eV, as shown by the ultraviolet visible (UV-vis) spectrometry results. The photon excitation energy varied between 2.65 eV and 1.76 eV with Ni^{2+} concentrations, according to photoluminescence (PL) studies. Dielectric properties, such as the dielectric constant and tangent loss, have been shown to vary with frequency. Generally speaking, the structure and characteristics of Sr_2MnWO_6 are successfully modified by the addition of Ni^{2+}, resulting in an appropriate band gap, low dielectric loss, and high dielectric permittivity.

Received 26th August 2025
Accepted 25th September 2025

DOI: 10.1039/d5ra06378g

rsc.li/rsc-advances

1. Introduction

Double perovskite oxides with the general formula $A_2BB'O_6$ have emerged as versatile materials with wide-ranging applications in microwave communication systems, dielectric resonators, sensors, and optoelectronics owing to their flexible crystal structure, tunable bandgap, biocompatibility, and excellent thermal and electrical stability.[1–6] These properties make them particularly attractive for developing next-generation electronic devices that require both high performance and reliability. As research continues to uncover new compositions and modifications, the potential for even broader applications in energy storage and conversion technologies is becoming increasingly evident.[7–9]

Among the broad family of double perovskites, tungstate-based compounds are capable materials because of their strong covalency of W–O bonds, which contributes to enhanced stability, reduced dielectric losses, and potential optical activity. In particular, the $Mn(Co_{1-x}Ni_x)_2WO_6$ system offers an exciting platform for investigation, as the substitution of Ni^{2+} at the Co^{2+} site introduces controlled changes in the ionic radius, electron configuration, and magnetic interactions. Such compositional tuning is expected to significantly influence the crystal structure, bandgap, dielectric response, vibrational modes, and magnetic properties of the material.[10,11] The intrinsic properties of the investigated materials are governed by the ordered distribution of Mn^{2+} and W^{6+} cations at the B-sites, which influence the electron hopping mechanism, lattice dynamics, and overall polarizability of the material.[10–15]

Tailoring the functional properties of Sr_2MnWO_6 (SMWO) ceramics through B-site substitution is a promising route for enhancing their performance in device applications. In particular, the substitution of Ni^{2+} ions for Mn^{2+} is of significant interest due to their similar ionic radii ($r_{Mn^{2+}}$ = 0.67 Å; $r_{Ni^{2+}}$ = 0.69 Å), allowing for isovalent replacement without introducing

[a]Department of Physics, Abdul Wali Khan University Mardan, 23200, Pakistan
[b]Department of Physics, Government Postgraduate College, Nowshera 24100, KP, Pakistan. E-mail: kasadiiui@gmail.com
[c]Center for Scientific Research and Entrepreneurship, Northern Border University, Arar 73213, Saudi Arabia
[d]Mechanical Engineering Department, College of Engineering, King Khalid University, Abha 61421, Aseer, Kingdom of Saudi Arabia
[e]Centre for Engineering and Technology Innovations, King Khalid University, Abha 61421, Aseer, Kingdom of Saudi Arabia
[f]Research Center for Advanced Materials Science (RCAMS), King Khalid University, Guraiger, P.O. Box 9004, Abha 61413, Aseer, Kingdom of Saudi Arabia
[g]Department of Physics, Riphah International University Islamabad, 44000, Pakistan. E-mail: zaman.abid87@gmail.com

severe lattice distortion.[16–21] Ni^{2+} incorporation is expected to influence the degree of cationic ordering, octahedral tilting, and electronic band structure, thereby modulating both the optical and dielectric properties, *i.e.*, relative permittivity (ε_r), and quality factor ($Q \times f$).[22–26] The optical properties, particularly the band gap energy (E_g), are sensitive to the d–d transitions and the charge transfer from oxygen 2p to metal cations, which are significantly affected by the nature of B-site cations. Ni^{2+} substitution can result in localized defect states or altered Mn–O–W super exchange interactions, leading to measurable shifts in E_g as observed through UV-vis diffuse reflectance spectrophotometry.[27,28] Similarly, the dielectric behavior is highly dependent on intrinsic structural factors such as grain size, density, porosity, and lattice strain, all of which can be manipulated *via* compositional changes and controlled sintering.[29–34] While several double perovskites have been studied for microwave applications, reports on Ni^{2+}-doped SMWO ceramics, especially with a comprehensive analysis of both optical and dielectric behavior, remain limited.

The motivation for this study lies in the ability of Ni^{2+} substitution to tailor the structural, optical, vibrational, and dielectric properties of SMWO. Understanding such modifications is essential for optimizing the material for applications in next-generation multifunctional devices. While several reports have focused on Mn- or Fe-based double perovskites, systematic exploration of Ni^{2+}-doped SMWO is still lacking, particularly with regard to its vibrational dynamics and dielectric response. Addressing this gap will provide new insights into structure–property correlations in double perovskites.

The present work aims to synthesize Ni^{2+}-doped SMWO *via* the solid-state route and to conduct a detailed investigation of its.

(i) Structural properties using X-ray diffraction (XRD) to confirm phase purity and lattice modifications.

(ii) Optical properties to evaluate band gap variations induced by Ni^{2+} substitution.

(iii) Vibrational properties through FTIR spectroscopy to probe local lattice distortions.

(iv) Dielectric properties as a function of frequency and temperature to understand polarization mechanisms.

We hypothesize that the incorporation of Ni^{2+} ions into SMWO will induce structural distortions and modify cation interactions, leading to observable changes in the optical band gap, vibrational modes, and dielectric behavior. These modifications are expected to enhance the multifunctional applicability of SMWO-based double perovskites.

2. Experimental methods

2.1 Synthesis of materials

Using a traditional mixed oxide method, $Sr_2Mn_{1-x}Ni_xWO_6$ ($0.00 \leq x \leq 0.40$) ceramic solid solutions were formed. The chemical precursors required in the current research were strontium carbonate ($SrCO_3$), manganese oxide (MnO_2), nickel oxide (NiO), and tungsten oxide (WO_3), with their scientific purity rate greater than 99%; these were blended instantaneously under a suitable molar ratio for 6 hours, and the powders were then subjected to horizontal ball milling, wherein they were placed in a polymeric bottle with zirconia balls as the grinding media and ethanol as the solvent. The mixture was kept in a beaker and then dried at 100 °C in a microwave oven. The dried powder was subjected to calcination at 800 °C for 6 h at a heating/cooling rate of 10 °C min^{-1} in an aluminum crucible. The calcined powder was smashed using a mortar and pestle to ensure a uniform mixture. The ultrafine and calcined powder was squeezed into a 10 mm-diameter pellet at a pressure of 100 MPa using a manual pellet press machine. The pellet samples were sintered for 6 hours at 950 °C, with a heating and cooling rate of 10 °C per minute. After being thoroughly polished, the sintered pellets were coated with gold to mitigate charging during SEM and microwave dielectric characterization.

2.2 Characterizations

The crystalline phases and lattice parameters of the sintered ceramics were examined using X-ray diffractometry (XRD, PANalytical X'Pert PRO) with Cu-Kα radiation ($\lambda = 1.5406$ Å) operating at 40 kV and 40 mA. The surface morphology and grain structure were studied using a scanning electron microscopy (SEM, JEOL JSM-6480LV). Utilizing an energy dispersive X-ray (EDX) machine (INCA200/Oxford, UK), the elemental composition was examined. Fourier transform infrared (FTIR) spectra were recorded in the 400–1000 cm^{-1} range using a PerkinElmer Spectrum Two FTIR spectrometer to identify vibrational modes and confirm metal–oxygen bonding characteristics. Ultraviolet-visible (UV-vis) diffuse reflectance spectra were obtained using a Shimadzu UV-2600 spectrophotometer equipped with an integrating sphere, and the optical bandgap energy was calculated using the Kubelka–Munk function. Photoluminescence (PL) spectra were recorded at room temperature by using a Horiba Jobin Yvon Fluorolog-3 spectrophotometer with a xenon lamp as the excitation source. The dielectric properties of the sintered ceramic samples were determined by using an impedance analyser (Agilent-E4991A) operating in the frequency range of 1 kHz to 2 MHz. Silver paste was applied to both sides of the pellets as electrodes, and the measurements were carried out using a temperature-controlled sample holder.

3. Results and discussion

3.1 X-ray diffraction (XRD) analysis

The phase purity, crystal structure, and microstructural characteristics of the $Sr_2(Mn_{1-x}Ni_x)WO_6$ ($0.00 \leq x \leq 0.40$)-sintered ceramics were investigated by using powder X-ray diffraction (XRD), as illustrated in Fig. 1. All samples exhibited sharp and well-defined diffraction peaks, corresponding to a single-phase double perovskite monoclinic phase indexed with JCPDS card no. 00-008-0490 and space group ($P2_1/n$). No secondary phases were detected, suggesting successful Ni^{2+} substitution at the Mn^{2+} site without altering the primary phase.[35] The prominent diffraction peaks were observed at 2θ values near 22°, 27°, 33°, 45°, 52°, and 56°, corresponding to the (101), (112), (200), (204), (215), and (312) crystal planes, respectively. The intensity of the diffraction peaks was slightly enhanced with increasing Ni^{2+}

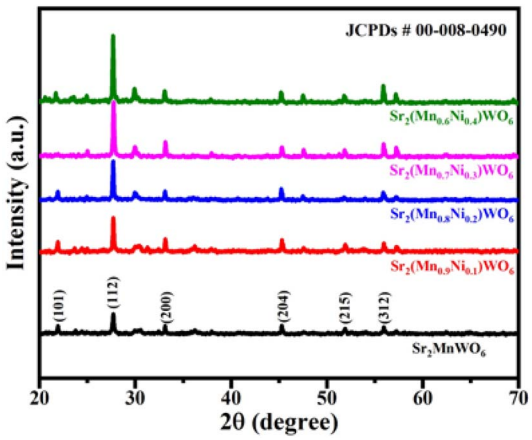

Fig. 1 XRD pattern of the $Sr_2(Mn_{1-x}Ni_x)WO_6$ ($0.00 \leq x \leq 0.40$)-sintered ceramics.

content, reflecting improved crystallinity and possibly grain growth. Table 1 lists the lattice parameters (a, b, c, β), unit cell volume (V), and other derived microstructural parameters. As the Ni^{2+} concentration increased, a gradual decrease in unit cell volume was observed. This contraction can be attributed to the smaller ionic radius of Ni^{2+} (0.69 Å) compared to Mn^{2+} (0.83 Å).[36,37] This change in unit cell volume indicates a substitutional effect where Ni^{2+} ions replace Mn^{2+} ions in the crystal lattice. Consequently, these structural modifications can influence the material's physical properties, paving the way for potential applications in advanced electronic devices.

The average crystallite size (D) was estimated using the Debye Scherrer equation;

$$D = \frac{0.9\lambda}{\beta \cos \theta} \quad (1)$$

In this case, β represents the 'full width at half maximum' (FWHM), θ is the Bragg's peak angular location in radians, $k = 0.9$ and λ is the wavelength (1.54 Å) of Cu Kα radiation.

Dislocation density (δ) and microstrain (ε) were calculated using the following relations:[38]

$$\delta = \frac{1}{D^2} \quad (2)$$

$$\varepsilon = \frac{\beta}{4 \tan \theta} \quad (3)$$

The structural parameters and microstructural parameters for all compositions have been listed in Table 1.

The results showed that increasing Ni^{2+} content led to a slight reduction in crystallite size and an increase in microstrain and dislocation density. The observed changes in lattice parameters, crystallite size, and microstrain reflect the sensitivity of the perovskite lattice to B-site cation substitution. These patterns are explained by substitutional induced defect generation and local lattice distortions.[39–41] These structural results serve as the foundation for additional optical and dielectric property studies, and validate the successful synthesis of the $Sr_2(Mn_{1-x}Ni_x)WO_6$ ($0.00 \leq x \leq 0.40$)-sintered ceramics *via* the solid-state reaction method.

3.2 SEM and EDX analysis

Fig. 2 and 3 show the SEM images and EDX spectra of the $Sr_2(Mn_{1-x}Ni_x)WO_6$ ($0.00 \leq x \leq 0.40$)-sintered ceramics, respectively. The SEM micrographs revealed densely packed grains with relatively uniform distribution and clear grain boundaries, indicative of good sintering behavior. With increasing Ni^{2+} content, a slight refinement in grain size was observed, which can be attributed to the substitutional effect of Ni^{2+} ions influencing the diffusion and grain growth kinetics during sintering. These results are consistent with prior reports on transition-metal doped double perovskites.[42,43] There is a noticeable change in grain size as the concentration of Ni^{2+} substitution rises. Because Ni^{2+} has a smaller ionic radius (0.69 Å) than Mn^{2+} (0.83 Å), the average grain size tends to gradually decrease as the Ni^{2+} content increases.[6] Internal lattice strain caused by this ionic substitution prevents grain development during sintering. Similar behavior has been shown in other double perovskite systems, including $Ba_2(Mn_{1-x}Ni_x)WO_6$ and $Sr_2(Mn_{1-x}Ni_x)WO_6$ ($0.00 \leq x \leq 0.40$).[18,20,33] Furthermore, the relatively dense packing of grains and the reduced grain boundaries with increasing Ni content are likely to impact the dielectric and optical properties by reducing defect scattering and enhancing charge carrier mobility. Grain size distribution analysis was performed *via* ImageJ software and estimated the grain size to be in the range of ~1–5 μm, depending on the substitution level. Lower Ni^{2+} content values exhibit coarser grains, while higher Ni^{2+} content values (*i.e.*, $x = 0.30$ and 0.40) show finer and more uniform grains. In perovskite ceramics, this pattern is consistent with the usual grain refinement effect of Ni^{2+} substitution. In addition to confirming that Ni^{2+} was successfully incorporated into the Sr_2MnWO_6 compound, these microstructural features suggest that Ni^{2+} substitution can be a useful method of microstructural tailoring to adjust the functional characteristics of these ceramics.

Table 1 Structural and microstructural parameters of the $Sr_2Mn_{1-x}Ni_xWO_6$ ($0.00 \leq x \leq 0.40$)-sintered ceramics obtained from XRD results

Composition (x)	Lattice parameters			FWHM, β (°)	Unit cell volume, V (Å^3)	Average crystallite size (nm)	Microstrain ($\times 10^{-3}$)	Dislocation density ($\times 10^4$ lines per m^2)
	a (Å)	b (Å)	c (Å)					
0.00	5.611	5.636	7.948	90.12	251.0	58	1.23	2.97
0.10	5.608	5.631	7.938	90.08	250.3	55	1.35	3.30
0.20	5.602	5.627	7.925	90.06	249.2	52	1.46	3.69
0.30	5.598	5.621	7.915	90.04	248.0	49	1.57	4.16
0.40	5.594	5.618	7.903	89.98	246.7	47	1.65	4.53

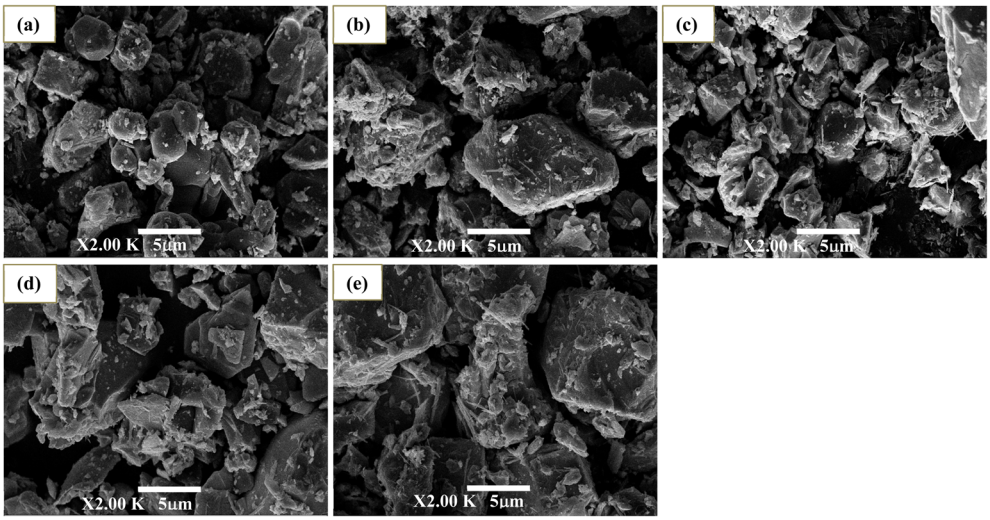

Fig. 2 SEM images of the $Sr_2(Mn_{1-x}Ni_x)WO_6$ ($0.00 \leq x \leq 0.40$)-sintered ceramics (a) 0.0, (b) 0.1, (c) 0.2, (d) 0.3, and (e) 0.4.

To complement the morphological analysis, EDX spectra were recorded to confirm the elemental composition and to verify the successful substitution of Ni at the Mn site. As shown in Fig. 3(a–e), all relevant elements, including Sr, Mn, W, O, and Ni, were detected in appropriate ratios corresponding to the nominal compositions. The EDX results for the undoped sample ($x = 0.00$) showed no presence of Ni, while progressively Ni-substituted samples exhibited increasing Ni content with a corresponding decrease in Mn content, thus confirming the site-specific substitution and compositional homogeneity. The detailed quantitative elemental compositions extracted from EDX spectra are tabulated in Fig. 3(a–e). Oxygen appeared as the major element due to its high atomic proportion in the ABO_6 double perovskite lattice. The presence of W^{6+} and Sr^{2+} remained nearly constant across all compositions, affirming their stability and non-participation in the substitutional mechanism.

The systematic variation of the Mn^{2+} and Ni^{2+} content with increasing x values validates the controlled substitution strategy used during synthesis. No foreign elements or impurity peaks were observed, confirming the phase purity of the synthesized ceramics. These observations affirm that Ni^{2+} ions have been successfully incorporated into the Sr_2MnWO_6 matrix without altering the fundamental elemental composition, and the microstructure remains compact and phase-pure throughout the substitution range.

3.3 FTIR spectrometry analysis

Fig. 4 shows the FTIR spectra of the $Sr_2(Mn_{1-x}Ni_x)WO_6$ ($0.00 \leq x \leq 0.40$)-sintered ceramics in the range of 4000–500 cm^{-1}, indicating several characteristics like the absorption bands and metal–oxygen stretching and bending vibrations. A broad absorption band observed around 3400–3500 cm^{-1} is attributed to the O–H stretching vibrations, indicating the presence of adsorbed water molecules or residual hydroxyl groups on the ceramic surfaces.[44] A shoulder appearing near 1630–1650 cm^{-1} corresponds to H–O–H bending vibrations, further confirming moisture absorption. In the lower wavenumber region (500–1000 cm^{-1}), several significant bands were recorded. The intense absorption band near 805–815 cm^{-1} is associated with the W=O stretching vibration, a typical feature of tungstate-based perovskites.[45] The bands around 620–680 cm^{-1} can be attributed to M–O (Mn/Ni–O) vibrations in the BO_6 octahedra, where M denotes Mn^{2+} or Ni^{2+}, and the shift in this band with increasing Ni^{2+} content suggests successful substitution of Ni^{2+} at the Mn^{2+} site.[46] A notable peak observed near 530–580 cm^{-1} is linked to Mn–O–Sr and Ni–O–Sr bending modes, which become more pronounced with increasing Ni^{2+} concentration, indicating increased structural distortion and changes in the local symmetry.[47] The systematic shift and change in intensity of these bands with increasing Ni substitution reflect the evolution of the local structure due to the substitutional incorporation of smaller Ni^{2+} ions (0.69 Å) compared to Mn^{2+} (0.83 Å).[48] These observations obtained from the FTIR spectra are listed in Table 2.

3.4 Photoluminescence (PL) spectrophotometry

Fig. 5 shows the PL spectra of the $Sr_2(Mn_{1-x}Ni_x)WO_6$ ($0.00 \leq x \leq 0.40$)-sintered ceramics at room temperature in the wavelength range of 400–800 nm. These peaks indicated the presence of radiative recombination processes associated with charge transfer and defect-related states. The major emission bands are centered around 468 nm, 516 nm, 564 nm, and 706 nm, corresponding to the photon energy of approximately 2.65 eV, 2.40 eV, 2.20 eV, and 1.76 eV, respectively. These values were calculated using the relation (4):

$$E = \frac{1240}{\lambda} \quad (4)$$

where 'E' is the photon excitation energy in electron volts and 'λ' is the emission wavelength in nanometers.

In the $[WO_6]^{6-}$ octahedra, the PL emissions are mainly linked to charge transfer transitions ($O^{2-} \rightarrow W^{6+}$) and intra-

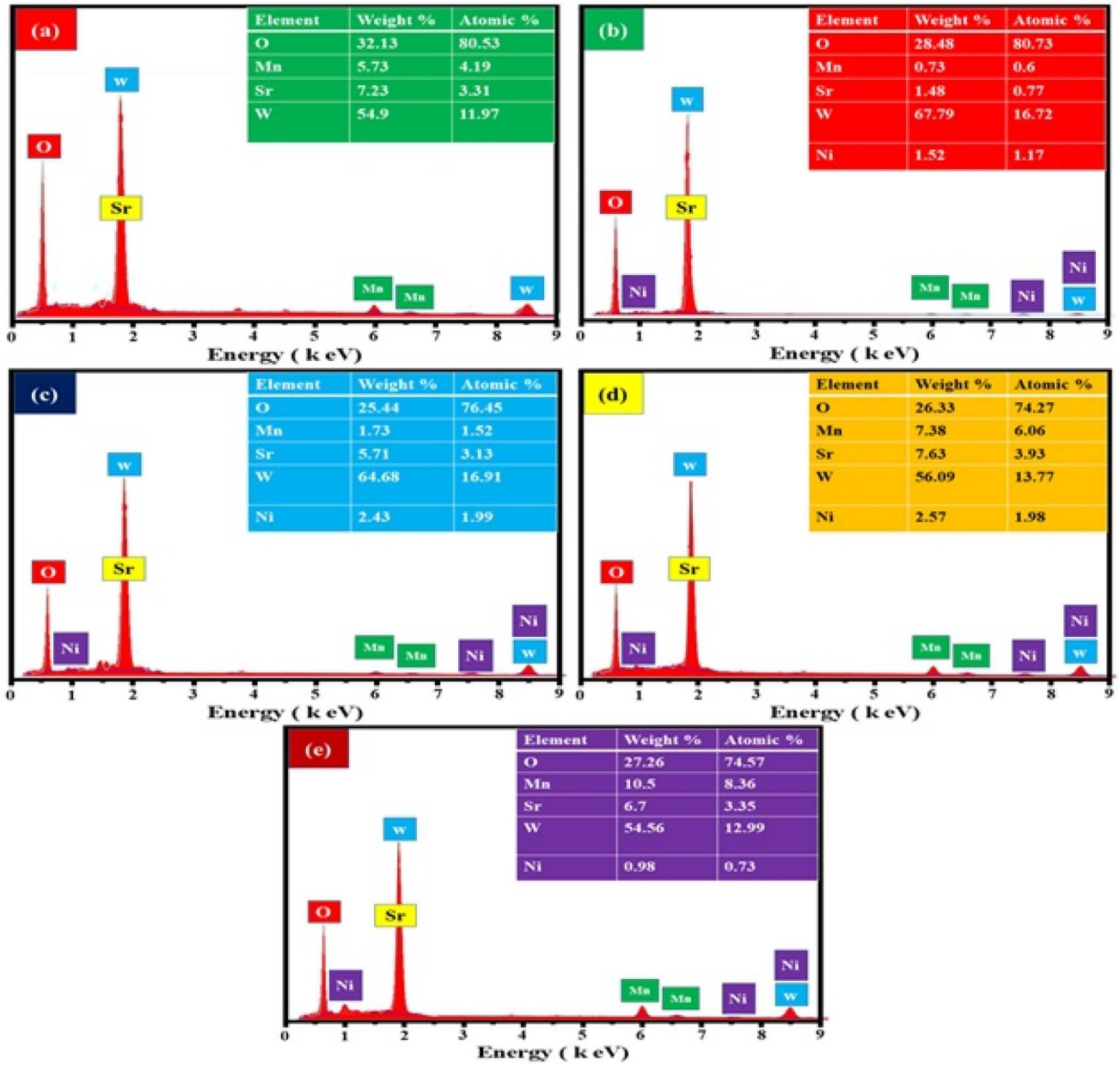

Fig. 3 EDX spectra of the $Sr_2(Mn_{1-x}Ni_x)WO_6$ ($0.00 \leq x \leq 0.40$)-sintered ceramics (a) 0.0, (b) 0.1, (c) 0.2, (d) 0.3, and (e) 0.4.

ionic d–d transitions, which result in higher energy emissions (468 nm and 516 nm). Deep-level trap states caused by Ni substitution at the Mn site, oxygen vacancies, and lattice defects are responsible for the reduced energy emissions between 564 nm and 706 nm. These explanations align with earlier research on double perovskites.[49–52] The introduction of non-radiative recombination centers is indicated by the gradual quenching of PL intensity that occurs with increasing Ni^{2+} substitution ($x = 0.10$ to 0.40). This is explained by enhanced carrier entrapment and lattice disorder brought on by the Ni^{2+} ions ($3d^8$), which change the local crystal field environment and produce more defect states. Moreover, minor peak shifts with increasing Ni content indicate perturbations in the local symmetry and crystal field splitting around the B-site octahedra (Mn/Ni). To better illustrate these transitions, the emission wavelengths and their corresponding photon energies are summarized in Table 3.

Assuming a typical excitation source wavelength of 325 nm, the corresponding excitation energy is approximately 3.81 eV, sufficient to induce electronic transitions from the O^{2-} 2p valence band to the W^{6+} 5d conduction band. This agrees with reported excitation mechanisms in similar tungsten-based perovskites.[53] Overall, the observed PL behavior highlights the effect of Ni^{2+} cation on the physical properties of Sr_2MnWO_6, where structural distortions and defect engineering offer potential tunability for optical and optoelectronic device applications.

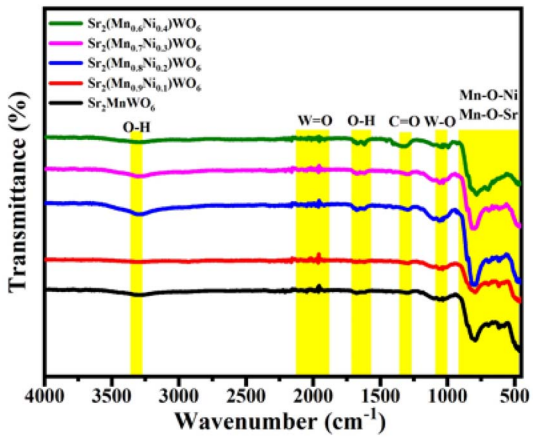

Fig. 4 FTIR spectra of the $Sr_2(Mn_{1-x}Ni_x)WO_6$ ($0.00 \le x \le 0.40$)-sintered ceramics.

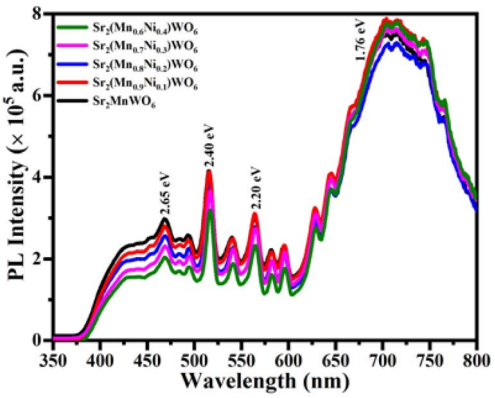

Fig. 5 PL spectra of the $Sr_2(Mn_{1-x}Ni_x)WO_6$ ($0.00 \le x \le 0.40$)-sintered ceramics.

3.5 UV-vis optical analysis

The optical absorption behavior of the $Sr_2(Mn_{1-x}Ni_x)WO_6$ ($0.00 \le x \le 0.40$)-sintered ceramics was investigated by UV-vis diffuse reflectance spectrometry (DRS) in the 200–800 nm wavelength range, as shown in Fig. 6.

All samples exhibited strong absorption in the UV region with a sharp absorption edge observed between 250 and 350 nm, indicative of intrinsic band-to-band transitions. Notably, the absorption edge exhibits a blue shift with increasing Ni^{2+} content, suggesting a systematic variation in the electronic structure induced by Ni^{2+} substitution at the Mn^{2+} site.

The optical band gap energies (E_g) of the samples were calculated by using the Tauc relation:[54]

$$(\alpha h\nu)^2 = A(h\nu - E_g) \quad (5)$$

where 'α' is the absorption coefficient, '$h\nu$' is the photon energy, 'A' is a constant, and 'E_g' is the band gap energy. The values of E_g are determined by extrapolating the linear region of the Tauc plots (Fig. 6(b)) to the energy axis at $(\alpha h\nu)^2 = 0$. The calculated band gap energies for the compositions, *i.e.*, Sr_2MnWO_6, $Sr_2(Mn_{0.95}Ni_{0.05})WO_6$, $Sr_2(Mn_{0.90}Ni_{0.10})WO_6$, $Sr_2(Mn_{0.85}Ni_{0.15})WO_6$, and $Sr_2(Mn_{0.60}Ni_{0.40})WO_6$, were found to be approximately 3.10 eV, 3.16 eV, 3.35 eV, 3.41 eV, and 3.51 eV, respectively.

The observed increase in band gap energy with Ni^{2+} substitution can be attributed to the modification in the electronic band structure caused by the partial substitution of Mn^{2+} with Ni^{2+} ions. These findings suggest that controlled Ni^{2+} substitution in Sr_2MnWO_6 allows for tunability of the optical band gap, making these materials suitable for UV-light-responsive applications such as photocatalysis, UV detectors, and optoelectronic devices.[55]

3.6 Dielectric properties

The frequency-dependent relative permittivity (ε_r) and dielectric loss ($\tan\delta$) of the $Sr_2(Mn_{1-x}Ni_x)WO_6$ ($0.00 \le x \le 0.40$)-sintered ceramics are illustrated in Fig. 7 and 8, respectively. A sharp decrease in ε_r and $\tan\delta$ is observed at low frequencies, stabilizing in the higher frequency region (above ~500 kHz), which is a characteristic response of dielectric materials with interfacial (Maxwell–Wagner) polarization behavior. This behavior is well explained by Koop's phenomenological theory and is commonly observed in heterogeneous ceramic systems.[1,23] The dielectric constant drops with increasing frequency because the molecular dipoles and charge carriers within the material cannot reorient and respond quickly enough to the rapidly alternating electric field, leading to reduced polarization. At lower frequencies, these mechanisms can effectively align with the field, but at higher frequencies, their inertia and the material's internal restraints prevent full alignment, making them less effective in storing energy and lowering the overall dielectric constant.[56]

The space charge and interfacial polarization at grain boundaries are the main causes of the high dielectric constant values at low frequencies (below 10 kHz). A considerable decrease in ε_r results from dipoles' inability to rapidly align with the alternating electric field as the frequency rises. The maximum ε_r (~360 at 1 kHz) is seen in the sample with $x = 0.40$

Table 2 FTIR peak assignments for the $Sr_2(Mn_{1-x}Ni_x)WO_6$ ($0.00 \le x \le 0.40$)-sintered ceramics

Wavenumber (cm^{-1})	Assignment	Description	References
~3450	O–H stretching	Adsorbed water/hydroxyl group	1
~1635	H–O–H bending	Physically adsorbed water	1
~815	W=O stretching	Tungstate group vibration	
~670	Mn/Ni–O stretching	BO_6 octahedral mode	3 and 4
~580	Mn–O–Sr/Ni–O–Sr bending	Bending vibration, structural distortion	4 and 5

Table 3 Calculated photon energies for the observed PL emission peaks of the $Sr_2(Mn_{1-x}Ni_x)WO_6$ ($0.00 \leq x \leq 0.40$)-sintered ceramics

S. no.	Emission wavelength (nm)	Calculated photon energy (eV)	Assigned transition/origin
1	468	2.65	Charge transfer transition within $[WO_6]^{6-}$
2	516	2.40	Intra-ionic transition (Mn^{2+}/Ni^{2+} related)
3	564	2.20	Defect-related or oxygen vacancy states
4	706	1.76	Deep level traps, possible Mn–O or Ni–O interactions

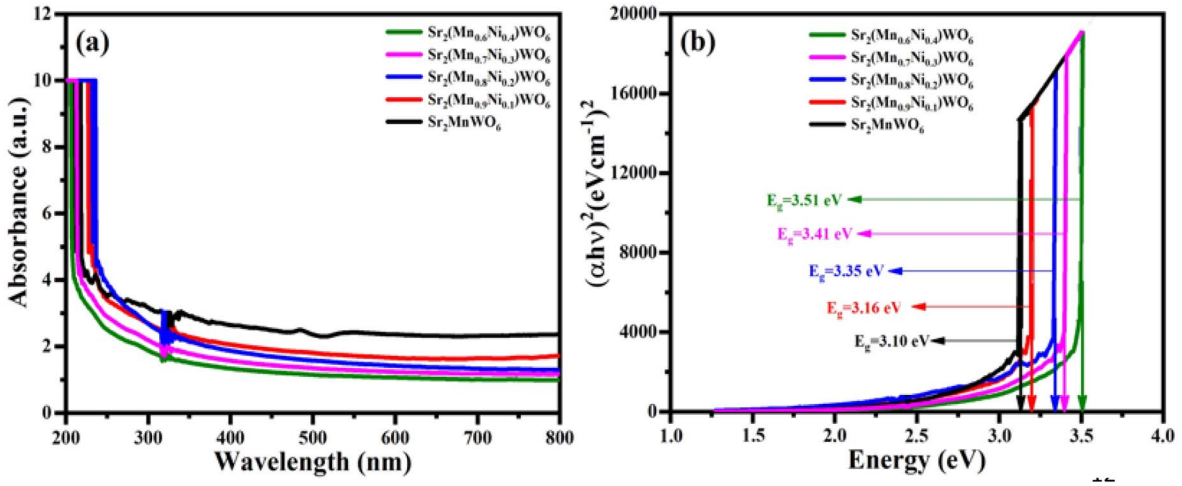

Fig. 6 (a) UV-vis spectra and (b) band gap energy of the $Sr_2(Mn_{1-x}Ni_x)WO_6$ ($0.00 \leq x \leq 0.40$) sintered ceramic.

($Sr_2(Mn_{0.6}Ni_{0.4})WO_6$), suggesting improved polarization as a result of Ni^{2+} inclusion, which provides mixed valence states and makes it easier for localized charge hopping between the Mn^{2+} and Ni^{2+} ions.[15,57] This pattern is supported by the behavior of the tangent loss (tan δ). Tan δ clearly decreases with frequency in all compositions, suggesting that energy dissipation is reduced at higher frequencies.

Remarkably, the $x = 0.40$ sample shows the lowest tan δ (~2 at 1 kHz), whereas the undoped SMWO has the greatest tan δ (~12 at 1 kHz). As demonstrated in the SEM micrographs, lower carrier dispersion facilitates dielectric relaxation, this decrease in dielectric strength in the presence of Ni^{2+} is ascribed to improved grain connection and decreased defect density.[49]

Overall, by raising ε_r and decreasing tan δ, Ni^{2+} substitution up to $x = 0.40$ improves dielectric performance. Because of this, SMWO is a good option for dielectric applications like microwave devices, resonators, and capacitors.

The presence of low-permittivity air in the voids causes greater dielectric losses and a drop in dielectric constant with frequency, as indicated by the SEM observation of porosity in the material. The total frequency stability of the material is further limited by this porous structure, which produces a frequency-dependent dielectric constant.[58,59] This phenomenon underscores the importance of optimizing the material's composition to minimize porosity and enhance its dielectric

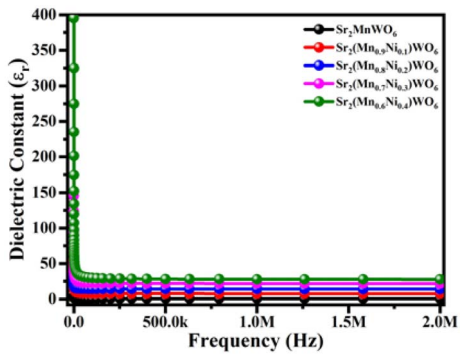

Fig. 7 Variation in ε_r with frequency of the $Sr_2(Mn_{1-x}Ni_x)WO_6$ ($0.00 \leq x \leq 0.40$)-sintered ceramics.

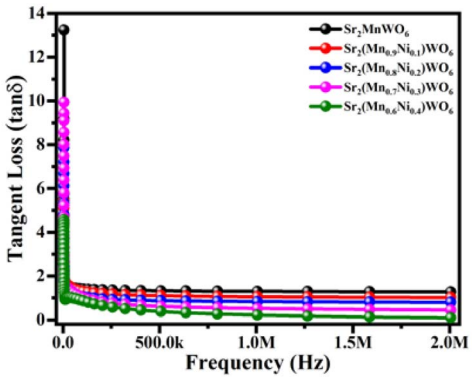

Fig. 8 Variation in tan δ with frequency of the $Sr_2(Mn_{1-x}Ni_x)WO_6$ ($0.00 \leq x \leq 0.40$)-sintered ceramics.

properties. Future research could focus on alternative materials or treatments that maintain structural integrity, while improving dielectric performance across a broader frequency range and densification through advanced sintering techniques, *e.g.*, hot pressing or spark plasma sintering could reduce dielectric losses. Such advancements could lead to the development of more efficient electronic devices, paving the way for innovative applications in telecommunications and energy storage. By leveraging advanced manufacturing techniques, researchers may be able to fine-tune the microstructure of these materials, resulting in enhanced performance and reliability.[60–63]

4. Conclusions

The $Sr_2(Mn_{1-x}Ni_x)WO_6$ ($0.00 \leq x \leq 0.40$) double perovskites were successfully synthesized by a mixed oxide route, and its structural, microstructural, optical, and dielectric properties were characterized. The following conclusions have been drawn from the results of the experiment:

(i) The materials' monoclinic (single-phase) structure and space group ($P2_1/n$) were determined by X-ray diffractometry (XRD).

(ii) SEM and EDX revealed relatively dense and homogeneous microstructures, although residual porosity was evident and contributed to dielectric losses.

(iii) The presence of infrared-active modes in the structure was confirmed by Fourier-transform infrared (FT-IR) spectroscopy, which showed multiple distinctive absorption bands linked to stretching and bending vibrations between the metal and oxygen.

(iv) Optical band gap values and photoluminescence spectra indicated electronic transitions consistent with Ni-induced modifications in the host lattice.

(v) A noticeable emission peak at 700 nm, which is suitable for generating red lasers, was discovered by photoluminescence spectroscopy. The photon excitation energy was 1.76 eV. Impedance analyzer spectrometry indicates that different forms of polarization cause dielectric characteristics to change with frequency.

(vi) Dielectric measurements showed frequency-dependent behavior with decreasing dielectric constant and improved stability at higher frequencies, which can be explained on the basis of Koop's two-layer model and space charge polarization.

Overall, the current study may be regarded as a basic inquiry that offers preliminary understanding of the function of Ni^{2+} substitution in SMWO. The obtained results lay the groundwork for next defect-level research and processing improvements meant to lower porosity, boost dielectric performance, and improve frequency stability for direct device-level applications.

Conflicts of interest

The authors declare no conflict of interest.

Data availability

The data will be made available on reasonable request.

Acknowledgements

The authors extend their appreciation to the Deanship of Research and Graduate Studies at King Khalid University, Kingdom of Saudi Arabia for funding this work through the Large Research Group Project under the grant number RGP.2/146/46. The authors extend their appreciation to the Deanship of Scientific Research at Northern Border University, Arar, KSA, for funding this research work through the project number "NBU-FFMRA-2025-2483-08".

References

1 M. T. Sebastian and H. Jantunen, Low loss dielectric materials for LTCC applications: a review, *Int. Mater. Rev.*, 2008, **53**(2), 57–90.

2 (*a*) D. Li, D. Jia, Z. Yang and Y. Zhou, Principles, design, structure and properties of ceramics for microwave absorption or transmission at high-temperatures, *Int. Mater. Rev.*, 2022, **67**(3), 266–297; (*b*) S. U. Din, H. Iqbal, S. Haq, P. Ahmad, M. U. Khandaker, H. O. Elansary and T. K. Z. El-Abedin, Investigation of the biological applications of biosynthesized nickel oxide nanoparticles mediated by Buxus wallichiana extract, *Crystals*, 2022, **12**(2), 146.

3 J. Varghese, N. Joseph, H. Jantunen, S. K. Behera, H. T. Kim and M. T. Sebastian, Microwave materials for defense and aerospace applications, in *Handbook of Advanced Ceramics and Composites*, Springer, 2019, pp. 1–48.

4 P. V. Tuza and M. M. Souza, B-cation partial substitution of double perovskite La2NiTiO6 by Co2+: Effect on crystal structure, reduction behavior and catalytic activity, *Catal. Commun.*, 2017, **97**, 93–97.

5 M. Nasir, A. K. Pathak, J. Kubik, D. Malaviya, V. Krupa, A. Dasgupta and S. Sen, Enhanced B-site cation ordering and improved magnetic properties: role of A-site Bi substitution in La2NiMnO6 double perovskites, *J. Alloys Compd.*, 2022, **896**, 162713.

6 A. Khalid, P. Ahmad, R. Memon, L. F. Gado, M. U. Khandaker, H. A. Almukhlifi and A. Timoumi, Structural, optical, and renewable energy-assisted photocatalytic dye degradation studies of ZnO, CuZnO, and CoZnO nanostructures for wastewater treatment, *Separations*, 2023, **10**(3), 184.

7 A. Khalid, P. Ahmad, A. Khan, A. A. Abdellatif, A. M. Abu-Dief, B. S. Al-Anzi and R. Ahmed, Development of CuO and CuO: Zn2+ nano-oxides for dye degradation and pharmaceutical studies, *Inorg. Chem. Commun.*, 2024, **160**, 111887.

8 B. Iqbal, Z. Sarfaraz, N. Muhammad, P. Ahmad, J. Iqbal, Z. U. H. Khan and A. Rahim, Ionic liquid as a potential solvent for preparation of collagen-alginate-hydroxyapatite beads as bone filler, *J. Biomater. Sci., Polym. Ed.*, 2018, **29**(10), 1168–1184.

9 R. D. Shannon, Revised effective ionic radii and systematic studies of interatomic distances in halides and

chalcogenides, *Acta Crystallogr., Sect. A:Found. Crystallogr.*, 1976, **32**(5), 751–767.

10 S. Mishra, R. N. P. Choudhary and S. K. Parida, Structural, dielectric, electrical and optical properties of a double perovskite: BaNaFeWO6 for some device applications, *J. Mol. Struct.*, 2022, **1265**, 133353.

11 Y. P. Wang, X. G. Li, X. G. Zhang, G. Christou and H. P. Cheng, Cation substitution effect on a molecular analogue of perovskite manganites, *J. Phys. Chem. C*, 2017, **121**(20), 10893–10898.

12 P. Zhang, J. Yang and S. H. Wei, Manipulation of cation combinations and configurations of halide double perovskites for solar cell absorbers, *J. Mater. Chem. A*, 2018, **6**(4), 1809–1815.

13 P. Ahmad, M. U. Khandaker, Z. R. Khan and Y. M. Amin, A simple technique to synthesize pure and highly crystalline boron nitride nanowires, *Ceram. Int.*, 2014, **40**(9), 14727–14732.

14 N. Muhammad, Z. Sarfraz, M. S. Zafar, S. Liaqat, A. Rahim, P. Ahmad and M. U. Khandaker, Characterization of various acrylate based artificial teeth for denture fabrication, *J. Mater. Sci.: Mater. Med.*, 2022, **33**(2), 17.

15 M. J. Winiarski, K. Kozieł, K. Sadecka and P. J. Dereń, The substitution effects on electronic structure of Ba2MgWO6 double perovskite oxide, *Solid State Commun.*, 2020, **314**, 113936.

16 J. Kui, Microwave dielectric ceramic materials and their industry development overview and future prospects, *J. Phys.:Conf. Ser.*, 2021, **1885**(3), 032034.

17 A. K. Azad, S. Ivanov, S. G. Eriksson, H. Rundlöf, J. Eriksen, R. Mathieu and P. Svedlindh, Structural and magnetic properties of the double perovskite Sr2MnWO6, *J. Magn. Magn. Mater.*, 2001, **237**(2), 124–134.

18 M. Nasarullah, P. Kanjariya, H. R. Manjunath, A. Kumar, S. Choudhury, A. K. Alqorashi and M. Faizan, Probing the Physical Properties of Double Perovskites Sr2ce (Ni, Sn) O6 Through First-Principles Investigations for Renewable Energy Applications, *SSRN*, 2025, 5227378.

19 M. J. Martínez-Lope, J. A. Alonso, M. T. Casais and M. T. Fernández-Díazb, Preparation, crystal and magnetic structure of the double perovskites Ca2TWO6 (T= Co, Ni), *Z. Naturforsch. B*, 2003, **58**(1), 127–132.

20 A. Khalid, P. Ahmad, A. Khan, M. U. Khandaker, I. Kebaili, M. M. Alam and D. Hayat, Cytotoxic and photocatalytic studies of hexagonal boron nitride nanotubes: a potential candidate for wastewater and air treatment, *RSC Adv.*, 2022, **12**(11), 6592–6600.

21 Y. Fujioka, J. Frantti and M. Kakihana, Franck− Condon Modes in Sr2MnWO6 Double Perovskite, *J. Phys. Chem. B*, 2004, **108**(44), 17012–17014.

22 C. Pughe, *Exploring the Effects of d10 and d0 Cations on the Magnetic Interactions in Perovskite Structures*, Doctoral dissertation, University of Sheffield, 2022.

23 R. A. Amel, Etude de premier principe des propriétés magnétiques, optoélectroniques et thermodynamiques des doubles pérovskites Ba2XWO6 (X: Ni, Co, Mn), Doctoral dissertation, Université Ibn Khaldoun-Tiaret, 2021.

24 X. Liang, K. Yamaura, A. A. Tsirlin and A. A. Belik, C a 2 CuW O 6: A triclinically distorted double perovskite with low-dimensional magnetic behavior, *Phys. Rev. B*, 2025, **111**(9), 094432.

25 A. Khalid, P. Ahmad, A. I. Alharth, S. Muhammad, M. U. Khandaker, M. R. I. Faruque and M. A. Alotaibi, A practical method for incorporation of Fe (III) in Titania matrix for photocatalytic applications, *Mater. Res. Express*, 2021, **8**(4), 045006.

26 I. A. Gorodeaa, F. G. Brezeanua, S. Trikib, K. Popaa, A. R. Iordana, M. N. Palamarua and A. Simionc, Contributions in Synthesis and Characterisation of the Double Perovskites Oxides in $Sr_2Fe(Mo_{1-x}W_x)O_6$ Series, *Acta Chem. Iasi*, 2009, **19**, 49–58.

27 Y. A. Alsabah, A. A. Elbadawi, M. Alsalhi, E. M. Mustafa and Y. Hajjah, Synthesis and study on the structural, optical and dielectric properties of Ba2Zn0. 75Ni0. 25WO6 new tungsten double perovskite, *Red Sea Univ. J. Basic Appl. Sci*, 2017, **2**(3), 25–39.

28 S. Afroze, A. M. Abdalla, N. Radenahmad, Q. C. Hoon Nam and A. K. Azad, Synthesis, structural and thermal properties of double perovskite NdSrMn2O6 as potential anode materials for solid oxide fuel cells. in *7th Brunei International Conference on Engineering and Technology*, 2018, (BICET 2018).

29 A. Correa, Study of the phonon spectrum of perovskites A_2NiBO_6 (A = Sr, Ba B = W, Mo) as a function of temperature, Doctoral dissertation, Universidade Federal do Maranhão, 2018.

30 N. Miniajluk-Gaweł, B. Bondzior, M. Ptak and P. J. Dereń, Highly sensitive temperature sensors resulting from the luminescent behavior of Sm3+-doped Ba2MgMoO6 high-symmetry double-perovskite molybdate phosphors, *Materials*, 2024, **17**(8), 1897.

31 I. A. Gorodea, Influence of the B-site cation nature on crystal structure and magnetic properties of Ca2BMoO6 (B= Cr, La, Sm) double perovskite, *Acta Chem. Iasi*, 2014, **22**(2), 145–154.

32 N. Miniajluk-Gaweł, B. Bondzior and M. Ptak, Dereń Exploring the Luminescence Behavior of Sm3+-Doped Ba2mgmoo6 High Symmetry Double-Perovskite Molybdate Phosphors, *SSRN*, 2023, 4657962.

33 M. Riaz, A. Suleman, P. Ahmad, M. U. Khandaker, A. Alqahtani, D. A. Bradley and M. Q. Khan, Biogenic synthesis of AgNPs using aqueous bark extract of Aesculus indica for antioxidant and antimicrobial applications, *Crystals*, 2022, **12**(2), 252.

34 D. Goman, Optimizacija hidrotermalne metode za sintezu složenih metalnih oksida na bazi mangana, Doctoral dissertation, Josip Juraj Strossmayer University of Osijek. Department of Chemistry, 2020.

35 A. Ali, A. Zaman, S. A. Aldulmani, M. Abbas, M. Mushtaq, K. Bashir and K. Althubeiti, Structural Evolution and Microwave Dielectric Properties of Ba1–x Sr x Ti4O9, ($0.0 \leq x \leq 0.06$) Ceramics, *ACS omega*, 2022, **7**(2), 2331–2336.

36 A. Pal, P. Singh, V. K. Gangwar, S. Ghosh, P. Prakash, S. K. Saha, A. Das, M. Kumar, A. K. Ghosh and S. Chatterjee, B-Site Disorder and Spin States Driven

Multiple-Magnetic Phases: Griffiths Phase, Re-Entrant Cluster Glass and Exchange Bias in Pr_2CoFeO_6, *Appl. Phys. Lett.*, 2019, **114**, 252403.

37 R. Saeed, A. Ali, T. Ahmad, A. Alhodaib, S. H. Alrefaee, S. Shomurotova and A. Zaman, Structural, optical, and dielectric properties of Sr2MWO6 (M= Ba, Mg, Zn, and Ca) double perovskites, *Ceram. Int.*, 2025, **51**(20), 31069–31076.

38 A. Zaman, S. Uddin, N. Mehboob and A. Ali, Structural investigation and improvement of microwave dielectric properties in Ca (HfxTi1-x) O3 ceramics, *Phys. Scr.*, 2020, **96**(2), 025701.

39 M. Tariq, M. A. Ali, A. Laref and G. Murtaza, Anion replacement effect on the physical properties of metal halide double perovskites Cs2AgInX6 (X= F, Cl, Br, I), *Solid State Commun.*, 2020, **314**, 113929.

40 J. Lv, Z. Cao, Y. Wang, F. Shi and J. Wang, Crystal structures and microwave dielectric properties of Sr2MgWO6 ceramics at different sintering temperatures, *J Materiomics*, 2022, **8**(1), 79–87.

41 K. Zheng, H. Wang, P. Xu, Q. Chen, B. Tu, W. Wang and Z. Fu, Investigation of the structural characteristics, dielectric properties, and infrared reflectivity spectra of AlON transparent ceramics, *J. Eur. Ceram. Soc.*, 2022, **42**(4), 1362–1369.

42 X. Guan, B. Zhang, Z. Wang, Q. Han, M. An, M. Ueda and Y. Ito, Natural polyphenol tannin-immobilized composites: rational design and versatile applications, *J. Mater. Chem. B*, 2023, **11**(21), 4619–4660.

43 R. D. Shannon, Revised effective ionic radii and systematic studies of interatomic distances in halides and chalcogenides, *Acta Crystallogr., Sect. A:Found. Crystallogr.*, 1976, **32**(5), 751–767.

44 A. Algahtani, S. Ali, T. Hussain, A. Ali, A. M. Quraishi, V. Tirth and A. Zaman, Studies on structural, optical and microwave dielectric properties of double perovskite Sr2Fe1+ xNb1-xO6, ceramics synthesized by solid state route, *Opt. Mater.*, 2024, **148**, 114822.

45 A. Gandhi and S. Keshri, Microwave dielectric properties of double perovskite ceramics Ba2Zn1−xCaxWO6 (x= 0−0.4), *Ceram. Int.*, 2015, **41**(3), 3693–3700.

46 J. J. Bian and J. Y. Wu, Structure and microwave dielectric properties of B-site deficient double perovskite–Ba [(Mg (1–x)/2Yx/3□ x/6) W1/2] O3, *Ceram. Int.*, 2016, **42**(2), 3290–3295.

47 Q. Chen, Y. Shen, H. Yan, Z. Zhao, R. Cai, Y. Yang and G. Dong, Transition Metal Ions-Doped Lead-Free Halide Double Perovskites for Stable Light Emission: Optical Properties and Optoelectronic Applications, *Adv. Mater. Technol.*, 2025, 2401997.

48 J. Yuan, Y. Zhang, J. Xu, T. Tian, K. Luo and L. Huang, Novel Cr3+-doped double-perovskite Ca2MNbO6 (M= Ga, Al) phosphor: Synthesis, crystal structure, photoluminescence and thermoluminescence properties, *J. Alloys Compd.*, 2020, **815**, 152656.

49 D. V. M. Paiva, Dielectric and photoluminescent investigation of Sr3MO6 (M= W or Mo) double perovskite electroceramic, Doctoral dissertation, Universidade Federal do Ceará, 2018.

50 S. Mohanty, S. Satapathy, M. Nayak, S. Rai, R. Singh and S. Behera, Effect of low Ni-substitution on optical, dielectric and magnetic properties of double perovskite Mg2FeNbO6, *Inorg. Chem. Commun.*, 2024, **165**, 112513.

51 S. Mishra, R. N. P. Choudhary and S. K. Parida, Structural, dielectric, electrical and optical properties of a double perovskite: BaNaFeWO6 for some device applications, *J. Mol. Struct.*, 2022, **1265**, 133353.

52 N. A. F. M. Saadon, N. M. Ali, N. Ibrahim and Z. Mohamed, Structural, optical and dielectric properties of Sr 2 Ni 1− x Mg x WO 6 (x= 0.00, 0.02, 0.04, and 0.06) double perovskite, *J. Mater. Chem. C*, 2021, **9**(38), 13439–13446.

53 A. Nazir, E. A. Khera, Z. Anjum, A. A. Ghfar, Y. A. Kumar and R. Sharma, Theoretical Engineering of Structural, Electronic, and optical characteristics of double Perovskite Sr2XWO6 (X= co, zn) for Optical devices, *J. Inorg. Organomet. Polym. Mater.*, 2025, **35**(1), 409–419.

54 F. Zhao, Z. Yue, Z. Gui and L. Li, Preparation, characterization and microwave dielectric properties of A2BWO6 (A= Sr, Ba; B= Co, Ni, Zn) double perovskite ceramics, *Jpn. J. Appl. Phys.*, 2005, **44**(11R), 8066.

55 S. Mohanty and S. Behera, Dielectric, electrical and optical properties of a Ni-substituted double perovskite ceramic, *Ferroelectrics*, 2024, **618**(1), 259–273.

56 H. Wang and L. Yang, Dielectric constant, dielectric loss, conductivity, capacitance and model analysis of electronic electroactive polymers, *Polym. Test.*, 2023, **120**, 107965.

57 J. Bijelić, D. Tatar, S. Hajra, M. Sahu, S. J. Kim, Z. Jagličić and I. Djerdj, Nanocrystalline antiferromagnetic high-κ dielectric Sr2NiMO6 (M= Te, W) with double perovskite structure type, *Molecules*, 2020, **25**(17), 3996.

58 O. Guillon, R. A. De Souza, T. P. Mishra and W. Rheinheimer, Electric-field-assisted processing of ceramics: Nonthermal effects and related mechanisms, *MRS Bull.*, 2021, **46**(1), 52–58.

59 M. Tokita, Progress of spark plasma sintering (SPS) method, systems, ceramics applications and industrialization, *Ceramics*, 2021, **4**(2), 160–198.

60 Y. Huang, K. Wu, Z. Xing, C. Zhang, X. Hu, P. Guo and J. Li, Understanding the validity of impedance and modulus spectroscopy on exploring electrical heterogeneity in dielectric ceramics, *J. Appl. Phys.*, 2019, **125**(8), 084103.

61 S. Halder, A. Dutta and T. P. Sinha, Dielectric relaxation and electrical conduction mechanism in A2HoSbO6 (A= Ba, Sr, Ca) Double Perovskite Ceramics: An impedance spectroscopic analysis, *J. Phys. Chem. Solids*, 2017, **102**, 79–89.

62 C. Ricca and U. Aschauer, Mechanisms for point defect-induced functionality in complex perovskite oxides, *Appl. Phys. A.*, 2022, **128**(12), 1083.

63 Z. K. Han, W. Liu and Y. Gao, Advancing the understanding of oxygen vacancies in ceria: Insights into their formation, behavior, and catalytic roles, *JACS Au*, 2025, **5**(4), 1549–1569.